

# CMB Spectrometer Concept and Science Case

Inflation probe: spectrometer working group

September 13, 2017

## 1 Overview of strawman concept

We present a strawman concept for a small spectrometer instrument as part of the PICO Probe concept study. The spectrometer is a Fourier transform spectrometer based on the PIXIE design, but using smaller beam-forming optics configured to produce a smaller beam on the sky. The sensitivity of a broad-band FTS scales as the square root of the etendue,  $A\Omega$ . With nominal primary mirrors 20 cm diameter and beam diameter 1 degree, the PICO spectrometer sensitivity is in the range 5–10% of the larger PIXIE spectrometer (primary mirror 50 cm diameter, beam size 2 degrees). Since the primary targets of interest (dust foreground for polarization, SZ effect for spectral distortions) could be detected at very high signal-to-noise ratio by PIXIE, the reduced sensitivity of the PICO spectrometer still allows substantial return for both science and foreground modeling.

## 2 Science case

### 2.1 $\gamma$ distortion and relativistic SZ

**Goal:** The Compton- $\gamma$  distortion is the largest expected CMB spectral distortion signal. It is dominated by contributions from the thermal Sunyaev-Zel’dovich (tSZ) effect sourced by galaxy groups and clusters at  $z \lesssim 2$ , but also receives contributions from diffuse gas in the intergalactic medium, the epoch of reionization, and energy release in the primordial plasma at  $z \lesssim 5 \times 10^4$  (e.g., from Silk damping of small-scale acoustic modes). Furthermore, the high temperature ( $\gtrsim$  keV) of the ionized gas in groups and clusters produces a relativistic tSZ signal that provides significant complementary information to that contained in Compton- $\gamma$ . These distortions directly measure the total thermal energy in electrons in our Hubble volume, as well as their  $\gamma$ -weighted temperature. Measurements of these quantities will provide precise answers to crucial astrophysical questions: what is the history of energy injection into intergalactic gas over cosmic time? What physical processes and timescales govern these “feedback” events? How do these processes alter the small-scale matter distribution? What types of sources were responsible for driving the epoch of reionization?

**Approach:** The global  $\gamma$ -distortion and relativistic tSZ (rtSZ) distortion can only be detected via a dedicated measurement of the monopole absolute sky intensity over a broad frequency range, with high sensitivity and good spectral resolution. The *COBE-FIRAS* limit,  $|\gamma| < 1.5 \times 10^{-5}$  (95% C.L.), is roughly one order of magnitude larger than the expected signal,  $\gamma \approx 1.77 \times 10^{-6}$  (Hill et al. 2015), of which  $\approx 90\%$  arises from groups and clusters. No limit on the rtSZ monopole signal has been derived from existing data. Forecasts for measurements of these signals, including marginalization over all of the most significant foregrounds, have been presented in Abitbol et al. (2017). The Compton- $\gamma$  distortion will be detected at high significance by a *PIXIE*-like instrument or a scaled-down spectrometer concept: the *PIXIE* detection significance is forecast to be  $\approx 200\sigma$  after foreground marginalization. The rtSZ distortion will be strongly detected by *PIXIE*, with a significance of  $\approx 10\text{--}15\sigma$  (depending on assumptions about external foreground information — with no external information, the significance is still  $\approx 5\sigma$ ). However, the detectability of the rtSZ signal with a significantly scaled-down spectrometer is currently under study. An optimization analysis to determine the minimum configuration needed for this detection is in progress. A rough estimate suggests that a five-fold increase over the *PIXIE* noise may still be sufficient for a  $3\sigma$  detection, given external information about low-frequency foregrounds.

The  $\gamma$  and rtSZ signals provide “integral constraints” on the injection of energy into intra- and intergalactic gas over cosmic time, similar to the constraint on the optical depth to reionization provided by large-scale CMB polarization measurements. The combination of the  $\gamma$  and rtSZ signals is extremely powerful in discriminating amongst models of energetic feedback, which drives galaxy evolution and strongly alters

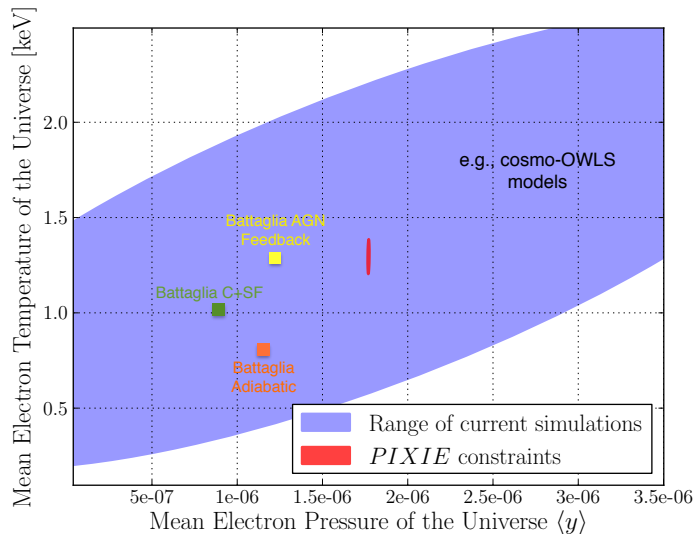


Figure 1: Range of current simulation predictions for the parameters probed by the  $y$ -distortion (mean electron pressure of the Universe; horizontal axis) and the rtSZ distortion (mean  $y$ -weighted electron temperature of the Universe; vertical axis) compared to the forecasted uncertainties for a *PIXIE*-like spectrometer (red ellipse). The light blue ellipse represents the range of theoretical predictions for these quantities, with individual model predictions denoted by the colored squares (Battaglia et al. 2012, Hill et al. 2015; cosmo-OWLS predictions provided by I. McCarthy). The vast range of predictions is driven by uncertainties in the implementation of feedback mechanisms in cosmological hydrodynamics simulations (e.g., from active galactic nuclei). Spectral distortion measurements will transform our understanding of these processes.

the small-scale matter power spectrum. Fig. 1 shows the current range of simulation predictions for these signals, as well as the forecasted *PIXIE* constraints. Even slightly weaker constraints than those shown here will dramatically improve our knowledge of the physical processes regulating galaxy formation and evolution. Moreover, the spectral distortion signals can be tomographically decomposed through cross-correlations with galaxy, quasar, and cluster catalogs, yielding important additional information about the history of energy injection.

Furthermore, these processes are deeply connected to the largest theoretical uncertainty faced by upcoming Stage-IV weak lensing surveys, namely, the effect of baryonic feedback on the small-scale matter power spectrum (e.g., Vogelsberger et al. 2014, Hopkins et al. 2014, Schaye et al. 2015). At face value, this uncertainty overwhelms the LSST baseline systematic requirements by more than an order of magnitude (Semboloni et al. 2011, Eifler et al. 2014). By directly constraining feedback physics with spectral distortion measurements, the CMB community can resolve this problem (which is also of potential relevance to future CMB lensing analyses).

The  $y$  and rtSZ distortions present additional scientific opportunities worthy of future exploration as well. With sufficient angular resolution ( $\lesssim 1$  degree), the stacked rtSZ signal can be used to calibrate the  $M$ - $T$  relation used as a cosmological probe in X-ray cluster analyses. In addition to the tomographic breakdown described above, cross-correlation of the  $y$  and rtSZ signals with deep galaxy and quasar catalogs can be used to remove the post-reionization signal, yielding direct constraints on the sources driving the process of reionization. Cross-correlation with future 21 cm data may even yield direct measurements of reionization. Lastly, the cross-power spectrum of  $y$  and CMB temperature fluctuation maps can be used to probe primordial non-Gaussianity on scales that have heretofore been inaccessible, with a cosmic-variance-limited sensitivity far exceeding that of the standard CMB temperature bispectrum estimator (e.g., Emami et al. 2015) also benefiting from using  $E$ -mode polarization (Ravenni et al., 2017).

## 2.2 $\mu$ distortion

In contrast to the Compton  $y$ -distortion,  $\mu$ -type or chemical potential distortions (Sunyaev & Zeldovich, 1970) can only be created in the primordial Universe at redshift  $z \gtrsim 5 \times 10^4$ , when Comptonization by free electrons was still very efficient. Detection of a  $\mu$ -type distortion would thus probe the thermal history

of the Universe at otherwise inaccessible regimes, opening a new window to the pre-recombination era. *COBE-FIRAS* constrained the  $\mu$ -distortion parameter to  $|\mu| \lesssim 9 \times 10^{-5}$  (Fixsen et al., 1996). Even today, this still stands as the best upper limit and directly limits any primordial energy release to the CMB to  $\Delta\rho_\gamma/\rho_\gamma \lesssim 6 \times 10^{-5}$ . In the past, this result was used to place independent limits on a wide range of physical process, including decaying particles (e.g., Sarkar & Cooper, 1984; Hu & Silk, 1993; Chluba & Sunyaev, 2012) and the amplitude of the small-scale power spectrum (Hu & Silk, 1993; Chluba et al., 2012).

With a *PIXIE*-type experiment, the bound of *COBE-FIRAS* could be improved by nearly three orders of magnitude, reaching  $|\mu| \lesssim \text{few} \times 10^{-7}$  (Abitbol et al., 2017). This would limit any source of energy release to  $\Delta\rho_\gamma/\rho_\gamma \lesssim 7 \times 10^{-8}$  at redshifts  $5 \times 10^4 \lesssim z \lesssim 2 \times 10^6$ . One natural and inevitable source of energy release is due to the damping of small-scale modes (at wavenumbers  $50 \text{ Mpc}^{-1} \lesssim k \lesssim 2 \times 10^4 \text{ Mpc}^{-1}$ ) set up by *inflation* or more general early-universe models responsible for the fluctuations seen at large angular scales through observations of the CMB temperature and polarization signals. The standard  $\Lambda$ CDM value of  $\mu \approx 2 \times 10^{-8}$  (e.g., Chluba et al., 2012; Chluba 2016) is currently out of reach (Abitbol et al., 2017); however, many alternative early-universe models exist that show enhanced power at small scales (e.g., running mass, waterfall and hybrid inflation models), while being fully compatible with CMB constraints obtained at large angular scales. In fact, some enhancement of the small-scale power spectrum amplitude could be required to explain the seeds for super-massive black holes found in the centers of almost any galaxy as well as the recently detected *LIGO* black hole mergers, which could both be of primordial origin (Kohri et al., 2014; Clesse & Garcia-Bellido, 2015). Alternative early-universe scenarios could be directly constrained using *any* improved  $\mu$ -distortion limit, thereby providing another crucial test of the slow-roll *inflation* paradigm that is driving many aspects of current cosmological research.

Although related to non-standard physics, improved  $\mu$ -distortion limits can also be interpreted in terms of particle physics. For long-lived decaying particles (e.g., excited states of dark matter, moduli or gravitinos) with lifetimes  $t_X \approx 10^9 - 10^{11}$  s, a *PIXIE*-type experiment could improve existing constraints derived from light element abundances (Kawasaki et al. 2005, 2017) by roughly one order of magnitude (Chluba & Jeong, 2013; Dimastrogiovanni et al., 2016). Similarly, new constraints on the interaction of dark matter particles with photons, neutrinos, electrons and proton can be derived using  $\mu$ -distortion measurements (e.g., Ali-Haïmoud et al., 2015; Diacoumis & Wong, 2017). A limit of  $|\mu| \lesssim \text{few} \times 10^{-7}$  could also be translated into bounds on *primordial magnetic fields*, *axion-photon interactions* and *super-conducting strings*, to name additional non-standard physics example (for overview see, Chluba, 2013; Sunyaev & Khatri, 2013; Tashiro 2014). For scale-down versions of *PIXIE*, the constraints are weakened by corresponding factors, with a natural threshold at  $|\mu| \lesssim \text{few} \times 10^{-6}$ , when decaying particle constraints from distortions no longer supersede those from light element abundances anywhere. This could still be reached with the minimal FTS concept considered here.

### 2.3 Intensity mapping, CIB

**Goal:** Intensity mapping (IM) allows us to understand average galaxy properties and their evolution in the context of  $\Lambda$ CDM. In particular for dusty galaxies: what halos best host star formation? How does star formation evolve relative to the growth of structure? What is the abundance, evolution and metallicity of the cold gas that forms stars? How does the mean dust temperature evolve?

**Approach:** Radiation from stars excites thermal emission from dust, and atomic and molecular line emission. A CMB spectral survey is sensitive to both the zero-point and anisotropy of the sum of re-processed radiation over the history of the universe. Cross-correlation of the spectral survey with galaxy redshift surveys separates the cumulative SED contributing to the CIB at each redshift (Serra et al. 2014, Switzer 2017). Cross-correlation between multiple frequencies identifies coherence in the CIB, and emission of different lines at common redshift (Serra et al. 2016). An estimate of the cross-correlation amplitude does not suffer cosmic variance, and is robust to galactic foregrounds.

Spectral resolution is essential to measuring redshifted line emission.  $C_\ell$  scales as  $\sim 1/\Delta$  (until 1% bandwidth, for fractional bandwidth  $\Delta$ ) as large-scale structure is washed out in thicker slabs (Breysse et al. 2014). CO and CII cannot be detected in WMAP data and CII has been tentatively detected in Planck (Pullen et al. 2017). A decisive measurement of evolution requires a spectrometer.

Spectral resolution and adjacency are essential to suppressing foregrounds: Foregrounds for CII can be 1000x larger than the signal. Dust emission is highly coherent between adjacent bands, while the IM signal is largely incoherent, so foregrounds can be removed efficiently with a linear combination of bands (Switzer 2017). Broad, separated bands make it more difficult to subtract the dust continuum. Foreground separation requires high interband-calibration smoothness and stability. A calibrator can be made black to  $3 \times 10^{-7}$  and is continuously differenced with the sky signal.

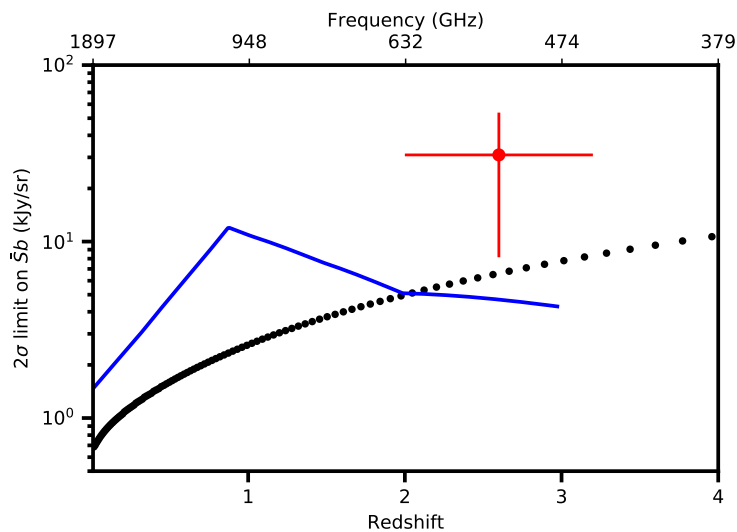


Figure 2: A spectrometer opens the possibility of studies of redshifted CII line emission. CII is the brightest cooling line, and maps of its redshifted intensity probe the star formation rate and large scale structure. A broadband CMB imaging survey washes out the density contrast from large-scale structure, and measurements from Planck 545 GHz x BOSS QSOs (Pullen et al. 2017, red point) provide a tantalizing first detection. Forecasts for CII emission from Uzgil et al. 2014 (blue) are nearly a factor of ten above the proposed spectrometer sensitivity for cross-correlation with a galaxy survey on 25% of the sky (black).

A spectrometer is better matched to galaxy surveys: Cross-correlations with galaxy redshift surveys provide unambiguous detection of CIB and line emission (Masui et al. 2013, Serra et al. 2014). Wide photometric bands are not well-matched to galaxy redshift surveys, which often provide many narrow slabs over a more limited redshift range. A spectrometer also potentially contains more redshift information, which is very useful to calibrate redshift estimation in photometric surveys such as LSST (Alonso et al. 2017).

A spectrometer with low angular resolution is not well matched to inference of SFR(M, z) from the CIB anisotropy (Wu, Dore 2017), and many factors of resolution are needed to be competitive, despite having a large number of bands. Its strength is in constraints of the integrated, monopole spectrum.

## 2.4 Zero level and absolute calibration

An absolute spectrometer has the capability to measure the zero-level of intensity maps, which an imager cannot do. This provides useful information for modelling foregrounds, not only in intensity (e.g. background level of radio and infrared sources, local diffuse foreground emission, which contributes to the lowest harmonic modes), but also for polarization (an absolute measurement of intensity is necessary to know the polarization fraction). The knowledge of the zero-level of maps is particularly useful at high galactic latitude, where the galactic foreground emission is faint.

An absolute spectrometer also provides an absolutely calibrated reference for the imager in many narrow frequency bands. Imager and spectrometer data can be combined by co-adding observations in several spectrometer bands to match the broader imager frequency bands (with proper weighting/interpolation to mimic the shape of the imager bands), and by convolving the higher angular resolution imager maps to match the coarser spectrometer resolution. Maps obtained in this way can be used to intercalibrate the imager and the spectrometer, and hence provide an alternative to the CMB dipole for the absolute calibration of imager channels. This is particularly important for frequencies above 400 GHz where the CMB dipole becomes too faint. This would allow constraining small frequency-dependent scattering signals (resonant and Rayleigh scattering), thus opening a way to constrain metals in the dark ages (Basu et al, 2004) and test recombination physics (Lewis, 2013). It would furthermore allow us to utilize the CMB imager to constrain anisotropic primordial  $\mu$  and  $\gamma$ -distortion signals, providing a test of scale-dependent non-Gaussianity (Pajer & Zaldarriaga, 2012; Biagetti et al., 2013; Emami et al. 2015; Ravenni et al., 2017).

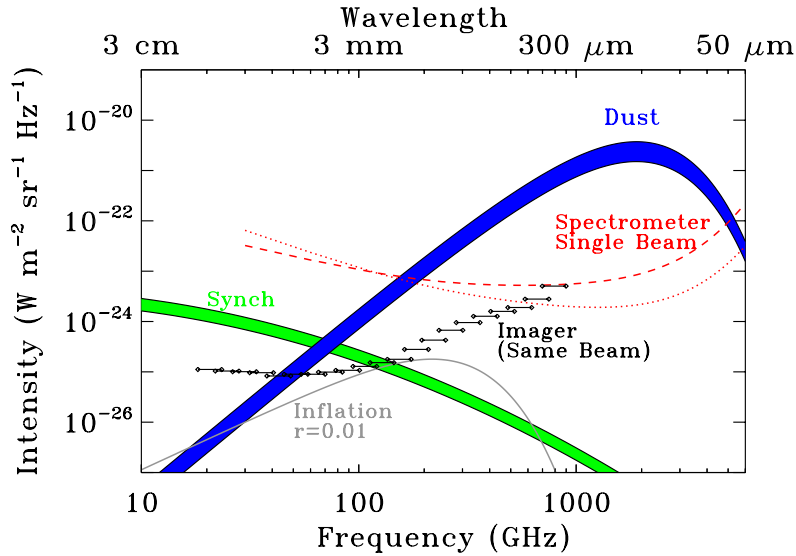


Figure 3: Sensitivity for the imager and spectrometer instruments compared to the CMB ( $r = 0.01$ ) and mid-latitude foregrounds. The imager sensitivity has been convolved to match the spectrometer angular resolution.

### 3 Foregrounds

Most of the sensitivity of the imager comes from channels between 90 and 190 GHz, where the dominant foreground emission is thermal dust. While thermal dust emission can be modelled empirically, to first order, with a modified blackbody emission (with pixel-dependent amplitude, temperature and spectral index), such a model can only be an approximation. The superposition of emissions from several regions along the line of sight mixes the emission of dust regions with different temperature, chemical composition, and physical environment (magnetic field, radiation field). In addition, alternate processes of emission are known to exist.

Emission from multiple dust components complicates foreground modeling and can introduce bias to CMB analyses. Spatial variation in the spectral energy distribution (SED) produces decorrelation of the foreground spatial distribution, restricting the choice of high signal-to-noise ratio “guard” channels for the imager. Using simple models of the dust spectra (one- or two-component fits to each line of sight) result in statistically significant bias if (as seems almost certain) the dust SED is differs from the model used in the foreground fit (Kogut 2016).

A spectrometer complements foreground subtraction for the imager by providing high signal-to-noise *spectra* of the dust emission along every line of sight. Information on the temperature distribution of the dust comes almost entirely from frequencies 1–2 THz where the dust emission peaks. Even a small spectrometer can determine the effective dust opacity as a function of temperature for dust temperatures 8–40 K typical for the diffuse dust cirrus. The resulting spectral/spatial data cube provides two main benefits to the imager: it provides an improved spectral basis to model the pixel-to-pixel spatial decorrelation of the dominant foreground component, while simultaneously providing a goodness-of-fit test for the dust SED assumed for foreground fitting by the imager.

Figure 3 compares the sensitivity of the spectrometer for a single 1-degree pixel to the sensitivity of the imager convolved to the same angular resolution. To compare the two instruments on an equal basis, the sensitivity for the imager has been re-scaled to the 1 degree beam size of the spectrometer. The channel width of the spectrometer is identical at all frequencies, so the fractional bandwidth of a single spectrometer channel is quite narrow ( $\Delta\nu/\nu = 10\%$  at 300 GHz, falling to 1% at 3 THz). The upper red plot shows the spectrometer sensitivity for a single beam and a single synthesized channel. The lower curve shows a more equal comparison with the imager, co-adding the spectrometer channels for a 25% fractional bandwidth.

The spectrometer is an excellent dust monitor. It has 64 channels with signal-to-noise ratio  $> 10$  per channel and per beam, compared to 12 for the imager. The integrated dust SNR for the spectrometer is more than four times that of the imager, and provides critical coverage across the peak of the dust spectrum to determine the dust opacity as a function of temperature.

Table 1 highlights the importance of high-frequency channels to fully characterize the dust SED in

### I. Imager Frequency Channels

CMB Bias in  $r$

	Input Model		
Fit Model	2-Temp	Multi	TLS
2-Temp	0.0	1.1E-5	0.015
Multi	2.2E-5	0.0	0.03
TLS	0.003	0.006	0.0

RMS Fractional Sky Residual  $\Delta I/I$

	Input Model		
Fit Model	2-Temp	Multi	TLS
2-Temp	0.0	1.9E-6	1.3e-4
Multi	1.3E-5	0.0	7.0E-4
TLS	2.8E-4	6.9E-4	0.0

### II. Spectrometer Frequency Channels

CMB Bias in  $r$

	Input Model		
Fit Model	2-Temp	Multi	TLS
2-Temp	0.0	0.40	1.7E-3
Multi	0.15	0.0	0.08
TLS	2.2	3.6	0.0

RMS Fractional Sky Residual  $\Delta I/I$

	Input Model		
Fit Model	2-Temp	Multi	TLS
2-Temp	0.0	0.42	0.08
Multi	0.25	0.0	0.02
TLS	11.2	2.1	0.0

Figure 4: CMB bias and fractional sky residual from fits to simulated sky spectra containing synchrotron, dust, and CMB. The fit uses either the imager frequency bands or the spectrometer frequency bands and compares the bias and residuals when the fit adopts the same dust model as the simulation input to the case where the fit adopts an incorrect dust model. Fits restricted to the imager frequency channels can produce significant bias in  $r$  without correspondingly large sky residuals (yellow). Mis-matched fits across the broader spectrometer frequency range can produce even larger bias in  $r$ , but also produce detectable sky residuals (green).

each beam. We generate simulated spectra containing synchrotron, CMB, and dust emission where the input dust emission is taken from one of three models. The first model is a modified blackbody with two temperature components (16K and 9K, following Finkbeiner et al. 1999 and Meisner & Finkbeiner 2015). The second model generalizes the dust to allow emission across a continuum of temperatures from 8K to 30K, adjusting the opacity at each temperature so that the integrated emission agrees with the Planck and FIRAS SEDs. The third model adopts the two-level system (TLS) emission of Paradis et al (2011), which produces a flattening of the dust spectral index at lower frequencies. We first evaluate the noiseless input spectra at the frequency channels for the baseline imager configuration, then fit for the synchrotron, dust, and CMB components using each of the three dust models in turn. When the fitting procedure adopts the same dust model as the input spectra (diagonal entries on the table matrix), the CMB term is correctly recovered. When the fitting procedure adopts an incorrect dust parameterization (off-diagonal entries), the fit produces a biased CMB result. However, the fit reproduces the combined sky emission to high accuracy ( $\Delta I/I < 10^{-5}$ ). Detecting the bias from goodness-of-fit criteria ( $\chi^2$ , etc) would require comparable  $10^{-5}$  SNR in the individual imager channels, substantially more than the SNR of the current baseline design.

We then perform a similar analysis using the spectrometer frequency channels. As before, adopting the correct dust model produces correct results, while the wrong model produces biased results. The difference now is that the broader spectrometer frequency coverage produces substantially larger sky residuals ( $\Delta I/I > 0.01$ ) for incorrect models, easily discriminating against biased fits. The combination of imager + spectrometer can combine the deep imager maps at CMB frequencies with the spectrometer data across the dust peak to discriminate competing dust models while yielding sufficient CMB sensitivity.